Published online 20 March 2019

Nucleic Acids Research, 2019, Vol. 47, No. 9 ***4843–4858***
doi: 10.1093/nar/gkz175

Interactions of p53 with poly(ADP-ribose) and DNA induce distinct changes in protein structure as revealed by ATR-FTIR spectroscopy

Annika Krüger[1,2,3,4], Anna Stier[1], Arthur Fischbach[1,3,4], Alexander Bürkle[1,*], Karin Hauser[2,*] and Aswin Mangerich[1,*]

[1]Department of Biology, University of Konstanz, Konstanz 78464, Germany, [2]Department of Chemistry, University of Konstanz, Konstanz 78464, Germany, [3]Konstanz Research School Chemical Biology, University of Konstanz, Konstanz 78464, Germany and [4]Zukunftskolleg, University of Konstanz, Konstanz 78464, Germany

Received January 06, 2019; Revised February 22, 2019; Editorial Decision March 01, 2019; Accepted March 08, 2019

ABSTRACT

Due to multiple domains and in part intrinsically disordered regions, structural analyses of p53 remain a challenging task, particularly in complex with DNA and other macromolecules. Here, we applied a novel attenuated total reflection Fourier transform infrared (ATR-FTIR) spectroscopic approach to investigate changes in secondary structure of full-length p53 induced by non-covalent interactions with DNA and poly(ADP-ribose) (PAR). To validate our approach, we confirmed a positive regulatory function of p53's C-terminal domain (CTD) with regard to sequence-specific DNA binding and verified that the CTD mediates p53–PAR interaction. Further, we demonstrate that DNA and PAR interactions result in distinct structural changes of p53, indicating specific binding mechanisms via different domains. A time-dependent analysis of the interplay of DNA and PAR binding to p53 revealed that PAR represents p53's preferred binding partner, which efficiently controls p53–DNA interaction. Moreover, we provide infrared spectroscopic data on PAR pointing to the absence of regular secondary structural elements. Finally, temperature-induced melting experiments via CD spectroscopy show that DNA binding stabilizes the structure of p53, while PAR binding can shift the irreversible formation of insoluble p53 aggregates to higher temperatures. In conclusion, this study provides detailed insights into the dynamic interplay of p53 binding to DNA and PAR at a formerly inaccessible molecular level.

INTRODUCTION

In response to DNA damage, rapid and complex cellular processes are triggered, which can result in DNA repair, transient or permanent cell cycle arrest, or apoptosis (1). Two key factors in the DNA damage response network are the tumor suppressor p53 and the DNA damage signaling enzyme PARP1, as well as its catalyzed reaction poly(ADP-ribosyl)ation (PARylation). As we have shown recently, the p53 and PARP1/PAR systems act in a close and interconnected molecular and functional relationship (2). Despite 40 years of research on p53, structural analyses of full-length p53—both, in its free state or in complex with other molecules—remain a challenging task with many open questions to be addressed (3). In the current study, we applied a novel attenuated total reflection Fourier transform infrared (ATR-FTIR) spectroscopic approach to analyze molecular mechanisms and consequences of the non-covalent interactions of p53 with its binding substrates PAR and DNA.

PARylation is a post-translational modification (PTM), which is formed shortly after the occurrence of several types of DNA lesions, in particular DNA strand breaks (4). Thereby, it is thought that PARylation supports and orchestrates the DNA damage response in higher eukaryotes (5). Besides its role in DNA repair, PARylation participates in transcription, cell cycle regulation, organization of subnuclear bodies, and regulation of cell death. PARP1 is the founding member of the PARP gene family, which consists of 17 homologs in humans, and synthesizes the majority of cellular PAR upon genotoxic stress (6). By consuming NAD^+ as a substrate, PARP1 can attach multiple ADP-ribose units via $1'' \rightarrow 2'$ ribose-ribose linkages onto proteins resulting in the formation of the nucleic-acid-like polymer PAR, which can consist of over 200 subunits. PARP1 can not only catalyze polymer elongation but also branching via

*To whom correspondence should be addressed. Tel: +49 7531 88 4067; Fax: +49 7531 88 4033; Email: aswin.mangerich@uni-konstanz.de
Correspondence may also be addressed to Karin Hauser. Tel: +49 7531 88 5356; Fax: +49 7531 88 3139; Email: karin.hauser@uni-konstanz.de
Correspondence may also be addressed to Alexander Bürkle. Tel: +49 7531 88 4035; Fax: +49 7531 88 4033; Email: alexander.buerkle@uni-konstanz.de

1‴ → 2″ ribose-ribose linkages, which leads to the formation of a heterogeneous mixture of PAR molecules (7). As a nucleic acid analog, PAR potentially forms secondary structures by base stacking and hydrogen bonds. Yet, data on this issue are inconsistent: although α-helical structures were postulated in previous studies using CD spectroscopy (8,9), this could not be confirmed via NMR studies (10). Apart from covalent PARylation of proteins, several modules were discovered in proteins, which can bind non-covalently to PAR. This includes macrodomains, PAR-binding zinc finger (PBZ) modules, WWE domains and PAR-binding motifs (PBMs) (11). While the structure and binding modes of macrodomains, PBZ modules and WWE domains are solved, the exact mechanism of the interaction of PBMs with PAR remains elusive. PBMs are short aa stretches with a loosely defined consensus sequence comprising a cluster rich in basic aa interspersed by hydrophobic residues (12).

p53 represents one of the most important tumor suppressor proteins, which is evident by the fact that it is dysregulated in >50% of all human cancers (13). As a transcription factor, p53 controls the expression of >500 target genes, many of which are involved in cellular stress response (14). p53 acts as a homotetramer, which is formed via its tetramerization domain (TET) as a dimer of dimers (Figure 1A). The primary dimers are formed via intermolecular β-sheets and helix packing interactions. The secondary dimers are stabilized via hydrophobic interactions between helices (15,16). Sequence-specific DNA binding to p53 response elements (RE), such as the p21 promoter element, is mainly mediated via the DNA binding domain (DBD) (Figure 1A). It consists of a central immunoglobulin-like β-sandwich. A loop-sheet-helix motif and two loops form the DNA binding surface (16,17). So far, no crystal structure of full-length p53 exists, as certain parts within the p53 protein such as the transactivation domain (TAD) and the C-terminal domain (CTD) are intrinsically disordered. Interestingly, via a multi-technique approach including small angle X-ray scattering, electron microscopy and NMR spectroscopy, it was shown that in its free state p53 has probably an open, cross-shaped structure with the tetramerization domain at its center and a pair of loosely coupled core domain dimers at the ends. Upon DNA binding, the structure closes around the DNA and becomes more compact (18). Although the CTD is intrinsically disordered, several NMR studies of CTD peptides reported disorder-to-order transitions upon binding to partner proteins. Binding of Ca^{2+}-loaded dimeric S100 protein resulted in an α-helical conformation (19) and binding of the bromodomain of the coactivator CBP induced a β-turn-like structure (20). In contrast, binding to DNA did not induce significant secondary structural elements, but local helix formation could not be excluded (21). Via molecular dynamic (MD) simulations of the CTD peptide a set of distinct structures was observed, including β-structures, 3_{10} and α-helical turns, coils and turns-containing structures (22). Nevertheless, the structure of the CTD in context of the full-length protein remains elusive.

The CTD exhibits crucial functions in the regulation of p53 at many levels, including DNA binding, cofactor recruitment and protein stabilization (2,3,23). On the one hand, it was postulated that the CTD has a negative regulatory function, as its deletion leads to activation of sequence-specific DNA binding (24). On the other hand, several subsequent studies reported a positive regulatory function by mediating fast scanning of the DNA and increased p53–DNA stability (23,25–27). The sequence-independent DNA binding of the CTD is mainly mediated via three lysine residues (K373, K381, K382) and can be attenuated via acetylation of those residues (21). Besides acetylation, the CTD is also a target of several other post-translational modifications including methylation, ubiquitination, sumoylation, neddylation and phosphorylation, all of which are affecting the regulatory function of p53. Recently, we discovered that p53 harbors a PBM-like region within the CTD, which renders a strong non-covalent interaction of p53 to PAR and auto-PARylated PARP1 (2) (Figure 1A). This specific and high-affinity non-covalent p53–PAR interaction determines substrate specificity for the subsequent covalent PARylation of p53 by PARP1 and had substantial implications on molecular and cellular levels.

Infrared (IR) spectroscopy is a highly-informative biophysical technique, which allows the label-free analysis of protein secondary structures in real-time under near-physiological conditions (28,29). The shape of the amide I band (between wavenumbers of 1720–1595 cm^{-1}) within the IR spectrum of a protein provides information on secondary structure elements like β-sheets (1623–1641 and 1674–1695 cm^{-1}), β-turns (1662–1686 cm^{-1}), α-helical (1648–1657 cm^{-1}), 3_{10}-helical (1660–1666 cm^{-1}), and disordered structures (1642–1657 cm^{-1}) (28,29) (Figure 1B). The exact position of each amide I band component depends on many factors including the extent of the respective secondary structure element, solvent accessibility and hydrogen bonding (28). Amyloid aggregates, for example, consist of strongly hydrogen-bonded extended β-sheets and are observed at lower frequencies (1611–1633 cm^{-1}) compared to native β-sheet proteins (28,30). Even though IR spectroscopy does not result in atomic resolution it is extremely powerful with regards to the analysis of subtle structural changes. ATR-FTIR spectroscopy is a measuring technique of IR spectroscopy, where the sample is analyzed on a crystal surface. The small penetration depth of light into the sample reduces the otherwise strong absorption signal of water, which overlaps the structure-sensitive amide I region of proteins. Such an approach allows a better subtraction of water signals from protein spectra providing an improved analysis of secondary structures in aqueous solutions.

Here, we performed a comprehensive study on structural changes of full-length p53 upon binding to PAR and DNA using a recently developed ATR-FTIR spectroscopic approach (31). Our method includes the passivation of the crystal surface with polyethylene glycol (PEG) to prevent unspecific protein adsorption and the specific immobilization of DNA or PAR, which increases the local surface concentration of the molecules of interest (Figure 1C). This approach allowed us to study the dynamic interplay of interactions of p53 with different DNA and PAR substrates providing formerly inaccessible structural information.

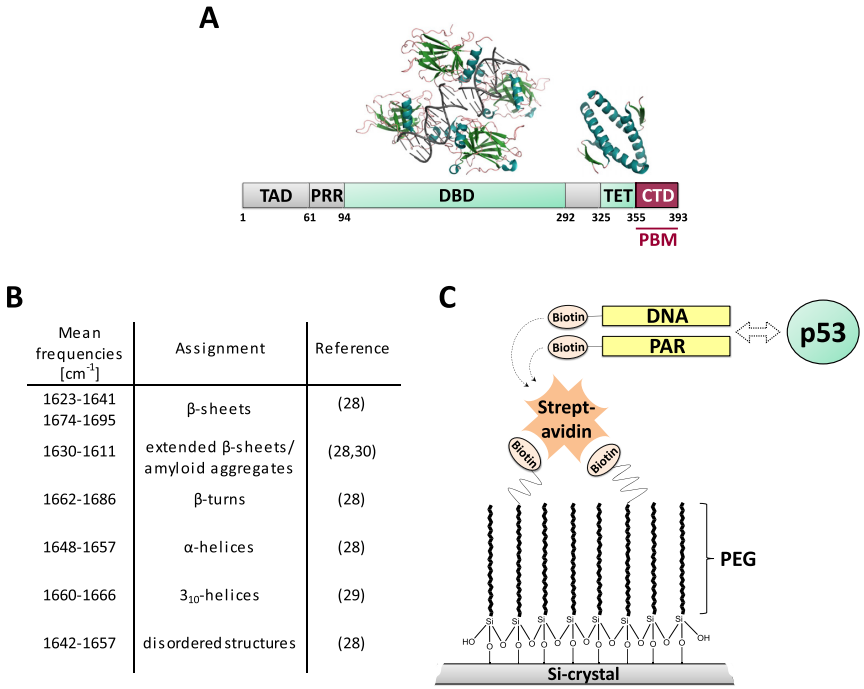

Figure 1. (**A**) Domain structure of p53 and localization of the PAR binding motif (PBM) as identified in (2). Structures of the DNA binding domain (DBD) in complex with DNA (PDB code: 2ahi (71)) and the tetramerization domain (TET) (PDB code: 2j0z (75)) are presented. The transactivation domain (TAD), the proline-rich region (PRR) and the C-terminal domain (CTD) are intrinsically disordered. (**B**) Secondary structure assignments of amide I band components. (**C**) Schematic representation of the ATR-FTIR spectroscopic approach. The silicon (Si) crystal is modified with polyethylene glycol (PEG) silane linkers to prevent unspecific protein adsorption. The local surface concentration of p53 is enhanced by immobilizing DNA or PAR via a streptavidin-biotin bridge. Modified from Krüger *et al.* (31).

MATERIALS AND METHODS

Protein purification

All purification steps were performed at 4°C using an ÄKTA FPLC system (GE Healthcare).

Purification of p53 variants. Purification of $p53^{WT}$, $p53^{1–355}$, $p53^{PBM4}$ (R363A, K370A, R379A, K381A) and $p53^{DBD-M}$ (R174A, R175A, H178A, R248A, R249A, R337A) was performed as described previously (2), with some modifications. Bacterial pellets [*Escherichia coli* strain BL21(DE3)] from 2 l cultures were resuspended in lysis buffer (50 mM Na-phosphate pH 8, 300 mM NaCl, 10 mM β-mercaptoethanol) supplemented with Complete EDTA-free protease inhibitor cocktail (Roche) and 1 mg/ml lysozyme (Sigma-Aldrich) and sonicated four times for 20 s. Then, 5 μg/ml DNase I (Roche) was added and samples were incubated for 1 h. Cell debris were removed by centrifugation (20 000 × *g*, 30 min) and the supernatant was filtered (syringe filter, 0.45 μm, Corning). After adding 10 mM imidazole, the filtrate was loaded onto a HisTrap HP column (GE Healthcare). After washing with 10 ml of 20 mM imidazole, p53 was eluted with 30 ml of 500 mM imidazole. The HisTag was removed via thrombin digestion (1 U/ml) during dialysis overnight (20 mM Na-phosphate pH 8, 100 mM NaCl, 1 mM β-mercaptoethanol). Thrombin digestion was stopped by the addition of 0.1 mg/ml Pefablock (Roche). Next, the samples were loaded onto a heparin HP column (GE Healthcare). Weakly bound proteins were removed by washing with 5 ml 200 mM NaCl. Elution was performed by a NaCl gradient up to 1 M (30 ml). p53 containing fractions were concentrated to 2–3 ml via centrifugal filters (Amicon Ultra 15, 10 kDa MWCO) and applied to size exclusion chromatography using a HiLoad 16/600 Superdex 200 column (GE Healthcare) (50 mM Tris pH 7.4, 300 mM NaCl, 1 mM DTT). The flow rate was set to 0.3 ml/min. p53 eluted in two peaks, of which only the fraction of the second peak was concentrated using a centrifugation device (Amicon Ultra 4, 10 kDa MWCO). The fraction of the first peak was discarded, as it contained high molecular-weight aggregates.

Purification of PARP1. PARP1 was purified as described previously (32), with some modifications. Briefly, bacterial pellets [*E. coli* strain Rosetta 2 (DE3)] from 2 l cultures were resuspended in lysis buffer (25 mM HEPES pH 8.0, 500 mM NaCl, 0.5 mM DTT, 10 mM benzamide) supplemented with 0.1% NP-40, Complete EDTA-free protease inhibitor cocktail (Roche) and 1 mg/ml lysozyme (Sigma) and sonicated four times for 20 s. Then, 5 μg/ml DNase I (Roche) was added and incubated for 1 h. Cell debris were removed by centrifugation (68 000 × *g*, 2 h), the supernatant was filtered (syringe filter, 0.2 μm, Corning) and loaded onto a HisTrap HP column (GE Healthcare). After washing with 10 ml of 1 M NaCl, PARP1 was eluted with 30 ml of 500 mM imidazole. The elution fraction was diluted to a final NaCl concentration of 375 mM NaCl with no-salt heparin buffer (50 mM Na-phosphate pH 7.0; 1 mM EDTA) and loaded onto a heparin HP column (GE Healthcare). PARP1 was eluted

by gradually increasing the NaCl concentration up to 1 M (30 ml). PARP1 containing fractions were concentrated and buffer was exchanged (50 mM Tris pH 8, 150 mM NaCl, 0.5 mM DTT) via centrifugal filters (Amicon Ultra 15, 10 kDa MWCO).

PAR synthesis and purification

For the synthesis and purification of PAR, a previously published protocol was adapted (33). The total amount of recombinant PARP1 protein from one purification was incubated at 37°C in a buffer containing 100 mM Tris (pH 7.8), 10 mM $MgCl_2$, 1 mM DTT supplemented with 300 μg/ml histone HIIa, 50 μg/ml *Eco*RI linker (GGAATTCC) and 1 mM NAD^+ in a total volume of 10 ml. After 45 min, the reaction was stopped with 10 ml 20% ice-cold TCA. After 15 min of incubation on ice, the sample was centrifuged (10 min, 9000 × *g*, 4°C). The pellet was washed twice with 1 ml ethanol and finally dried with a nitrogen flow. To separate PAR from proteins the pellet was resuspended and incubated for 10 min at 37°C under alkaline conditions (0.5 M KOH, 50 mM EDTA). Then, the pH was immediately adjusted to 7.5–8. The sample was supplemented with 50 mM $MgCl_2$ and 50 μg/ml DNase I and incubated for 2 h at 37°C. Proteins were digested overnight by the addition of 1 mM $CaCl_2$ and 50 μg/ml proteinase K. The next day, PAR was purified via two cycles of phenol/chloroform/isoamylalcohol (25:24:1) (Roth) extraction. In a last step residual phenol was removed via mixing the sample with chloroform. The aqueous phase was collected, and PAR was precipitated by the addition of 70% ethanol and incubation at -20°C overnight. The pellet was dissolved in water and the PAR concentration was determined by measuring the absorbance at 258 nm ($\varepsilon = 13500\ M^{-1}\ cm^{-1}$).

Biotinylation of PAR

PAR was labelled via EZ-Link Alkoxyamine-PEG4-Biotin (Thermo Fisher), which forms an oxime bond at the terminal ribose of PAR. Therefore, 3.7 mM of PAR was incubated in 100 mM Na-phosphate buffer (pH 7.0) supplemented with 5 mM EZ-Link Alkoxyamine-PEG4-Biotin in a total volume of 400 μl for 4 h at RT. To remove unreacted alkoxyamine the sample was dialysed overnight in 100 mM Na-phosphate buffer (pH 7.0). Labelled PAR fractions were purified via the Pierce Monomeric Avidin kit and concentrated via centrifugal filters (Vivaspin 2, 2 kDa MWCO).

Size-fractionation of biotinylated PAR

Biotinylated PAR chains were fractionated according to chain length by HPLC (Agilent 1100) equipped with a DNA Pac PA-100 column (Thermo Fisher). The column was equilibrated with 25 mM Tris (pH 9). Elution was performed by increasing the NaCl concentration (25 mM Tris, pH 9, 1 M NaCl) using the following program: 0–3 min 20%, 3–20 min 35%, 20–40 min 42%, 40–70 min 47%, 70–110 min 53%, 110–120 min 61%, 120–131 min 70%, 131–132 min 100%. Fractions were concentrated, and buffer was exchanged (20 mM Na-phosphate buffer, pH 7.0) via centrifugal filters (Vivaspin 2, 2 kDa MWCO).

ATR-FTIR spectroscopy

Measurements were performed with a Vertex 70V spectrometer (Bruker) equipped with a BioATR cell II (Bruker), which contains a multi-reflection silicon crystal with a light penetration depth of ∼850 nm at 1000 cm^{-1}. The spectral resolution was set to 4 cm^{-1}, and for each spectrum 100 scans were performed. The temperature of the crystal was controlled via an external water bath and set to 20°C. Before each measurement the sample chamber was purged for 20 min with dry air to eliminate water vapor. All measurements were performed in Tris buffer (50 mM Tris, pH 7.4, 150 mM NaCl).

Surface passivation of the ATR crystal. The modification of the crystal surface was performed as described recently (31). Briefly, the surface was activated by treatment with H_2SO_4 and H_2O_2. Next, the crystal was heated to 50°C and 20 mg/ml PEG-silane-biotin linker (5 kDa, Rapp Polymere) in 30 mM sodium acetate solution (pH 5.5) was added. After 30 min of incubation, the crystal was adjusted to 20°C and the biotin–PEG–silane linker solution was allowed to dry to achieve condensation of the silane groups. Then, the surface was washed thoroughly with MilliQ water and incubated in water over night. The next day, the crystal was washed thoroughly with Tris buffer and the spectrum of the modified surface was set as background.

Immobilization of biotinylated DNA/PAR. 20 pmol of biotinylated double stranded p53 response element from the p21 promotor (DNA_{RE}) (FWD: Biotin-CGAGGAAC ATGTCCCAACATGTTGCTCG AG), the scrambled version DNA_{scrRE} (FWD: Biotin-GTCGCTGACCCGAGAC TAGGCGTTCAAATA) or PAR was premixed with 10 pmol of streptavidin in 10 μl Tris buffer. The sample was applied to the biotinylated surface and incubated until the maximum signal was reached. This procedure was repeated until no further increase of signal was observed. The crystal was washed thoroughly with Tris buffer and the IR spectra of immobilized DNA/PAR were set as background.

Binding of p53 variants to immobilized DNA/PAR. p53 (100 pmol) was added in 20 μl to the immobilized DNA/PAR. After 20 min of binding reaction, a buffer exchange was performed. Then, the crystal was washed three times with a high salt buffer (50 mM Tris, pH 7.4, 500 mM NaCl) and the buffer was again exchanged with Tris buffer.

Interaction studies of p53 with DNA and PAR. The p53 variants were allowed to bind for 20 min to immobilized DNA/PAR and the buffer was exchanged once. In case of immobilized DNA, 2500 pmol PAR (concentration refers to ADP-ribose units) was added to a final volume of 25 μl. In case of immobilized PAR, 40 pmol of double-stranded DNA oligonucleotides (amount of nucleotides: 2400 pmol) were added to final volume of 25 μl. Competitive binding was allowed for 30 min. Then, the crystal was washed three times with a high salt buffer (50 mM Tris, pH 7.4, 500 mM NaCl) and the buffer was again exchanged with Tris buffer.

Spectral analysis. To analyze the binding of $p53^{WT}$, $p53^{PBM4}$ and $p53^{1–355}$ to DNA/PAR the IR signal of immo-

bilized DNA/PAR was set as background. Binding efficiencies were evaluated by normalizing the p53 signal to the signal of immobilized DNA/PAR. Therefore, the area of the amide I band of p53 (1720–1595 cm^{-1}) was divided by the area of characteristic DNA/PAR bands. In case of DNA, the streptavidin spectrum was subtracted from the spectrum of immobilized DNA and the area of 1740–1640 cm^{-1} was calculated. In case of PAR, the area of 1150–1010 cm^{-1} was calculated. The DNA/PAR binding studies were performed in two independent experiments and mean/SEM were calculated. To analyze structural changes between different p53 variants and different binding partners, the spectra were first corrected for different water content in the samples since a water band (OH-bending) interferes with the amide I band. Then, spectra were normalized to the area of the amide I bands and difference spectra were calculated to extract structural differences as indicated below.

CD spectroscopy

CD spectra were recorded with a Jasco-J815 spectrometer using a quartz cell with a path length of 0.1 cm. Five scans were accumulated at a scanning speed of 100 nm/s and a wavelength interval of 0.1 nm. Spectra were measured from 300 to 190 nm. Measurements with p53 variants (in a concentration of 4 μM, each) were performed in Tris buffer (50 mM Tris, pH 7.4, 150 mM NaCl). DNA_{RE} was added to a final concentration of 2 μM and unfractionated PAR to a final concentration of 120 μM (concentration refers to ADP-ribose units). Melting curve experiments were performed from 20°C to 90°C (1°C/min). Spectra were collected in 5°C steps. Two independent experiments of $p53^{WT}$ in the absence or presence of PAR/DNA_{RE} and $p53^{PBM4}$ and $p53^{1–355}$ were performed, respectively.

RESULTS

The C-terminal domain of p53 is a positive regulator of DNA binding

To analyze the role of the CTD of p53 in the context of sequence-specific DNA binding, we immobilized the p53 response element of the p21 promoter (DNA_{RE}) on the ATR crystal surface (Figure 1C) and compared the binding characteristics of different p53 variants. This included full length $p53^{WT}$, a PAR binding-deficient mutant with four basic aa exchanged to alanine in the CTD (i.e., $p53^{PBM4}$), and a C-terminally-truncated variant (i.e., $p53^{1–355}$), which is also PAR-binding deficient (2). The efficient immobilization of DNA_{RE} was examined via characteristic IR absorption bands including the antisymmetric (ν_{as}) and symmetric (ν_s) phosphate vibrations of the DNA backbone at 1222 and 1086 cm^{-1}, respectively (Supplementary Figure S1A) (34). The binding of p53 to the immobilized DNA was exerted in three stages: First, p53 was added and binding was allowed. Second, the buffer on the modified crystal surface was exchanged once to remove unbound or weakly bound p53; and in a final step, the crystal surface was washed with 500 mM NaCl (i.e. 'high salt wash') to disrupt the electrostatic interaction between p53 and DNA and thereby to examine the reversibility of the interaction (Figure 2A and Supplementary Figure S1B). When comparing DNA binding of different p53 variants, the strongest signal was observed for $p53^{WT}$, followed by $p53^{PBM4}$ (reduced by ∼30% compared to $p53^{WT}$), and the lowest signal was observed for $p53^{1–355}$ (reduced by 60% compared to $p53^{WT}$) (Figure 2A). This indicates that the sequence-specific DNA binding ability of p53 is not only dependent on its DNA binding domain (DBD), but also partially on the CTD. These observations support the theory of a positive regulatory function of the CTD, as reported previously (35). Since the exchange of four basic aa to alanine in $p53^{PBM4}$ showed an impact on the specific DNA binding ability of p53, it is likely that the electrostatic interactions of the positively charged aa of the CTD with the negatively charged DNA backbone contribute to the binding. After exchanging the buffer, the intensity of the amide I band of $p53^{WT}$ did not change significantly, confirming the strong interaction of full length $p53^{WT}$ to its DNA response element (Supplementary Figure S1B). In contrast, the intensities of the amide I bands of $p53^{PBM4}$ and $p53^{1–355}$ were reduced by about 25% after buffer exchange, which supports the notion that the CTD supports the sequence-specific DNA binding ability of p53. After a 'high salt wash' of the crystal, most of the p53 protein was removed, demonstrating the reversibility of the binding. Analyzing the amide I band of $p53^{WT}$ bound to DNA_{RE} provides information on the secondary structures of p53, as previously shown for other proteins (28,29). The second derivative of the amide I band was used for spectral analysis, as it resolves the overlapping components within the amide I band, which are caused by different secondary structures (Figure 2B). As expected, p53 bound to DNA_{RE} displayed a mixture of secondary structure elements, including β-sheet structures (1685, 1637 and 1623 cm^{-1}), β-turns (1673 cm^{-1}), as well as α-helical or disordered structures (1651 cm^{-1}). To elucidate the impact of the CTD on the secondary structure of p53 bound to the immobilized DNA_{RE}, we compared the shapes of the amide I bands of the p53 variants (Figure 2C–F). All p53 variants displayed largely comparable band shapes, indicating that the overall structures of the variants remained basically stable (Figure 2C and E). This is expected, since the CTD represents only approximately 10% of the full-length protein and any potential structural differences can be assumed to be small – yet potentially of functional significance - compared to the overall structure. For the purpose of analyzing such subtle structural changes, IR spectroscopy develops its full analytical power, because it is highly sensitive and slightest structural changes can be resolved by spectral subtraction (28,36). By generating difference spectra, all vibrational modes that showed no differences between the variants upon DNA binding, were cancelled out. Spectra of $p53^{PBM4}$ and $p53^{1–355}$ were subtracted from spectra of $p53^{WT}$, respectively, resulting in positive bands for secondary structures, which were more frequent in the WT protein, and negative bands for secondary structures, which were more frequent in the respective CTD variant. Interestingly, the difference spectra of $p53^{WT}/p53^{PBM4}$ as well as $p53^{WT}/p53^{1–355}$ showed a moderate, yet clear, negative difference band at ∼1625 cm^{-1} representing a structural component that is additionally present in the CTD variants, but not in WT (Figure 2D and F). This difference band can be

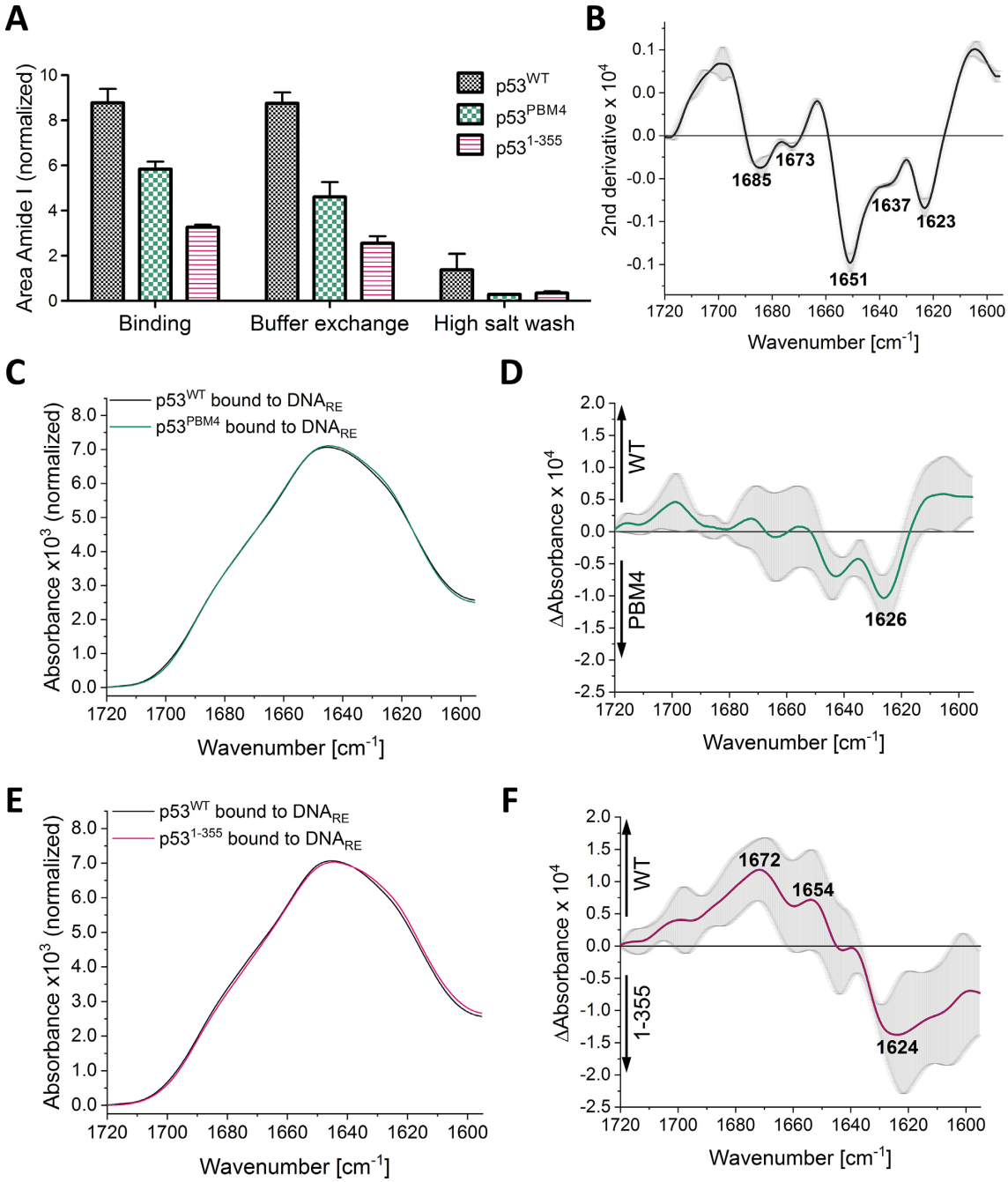

Figure 2. The CTD of p53 positively regulates binding to the p53 response element of the p21 promoter (DNA_{RE}) with distinct effects on secondary structure. (**A**) Evaluation of p53 binding by calculating the areas of the amide I bands and normalizing them to the immobilized DNA. First, p53 variants were added to the immobilized DNA_{RE} ('binding'), second, the buffer was exchanged to remove unbound protein ('buffer exchange'), and finally, the surface was washed with 500 mM NaCl to test the reversibility of the binding ('high salt wash'). (**B**) Second derivative of the amide I band exemplarily shown for $p53^{WT}$ bound to DNA_{RE}. (**C**) Representative amide I bands of $p53^{WT}$ and $p53^{PBM4}$, both bound to DNA_{RE}. Spectra are normalized to the area of the amide I bands. (**D**) Difference spectrum of $p53^{WT}$ and $p53^{PBM4}$ bound to DNA_{RE}. Average curve (green) and standard deviation (grey) of 16 difference spectra were calculated (combinations of four spectra of $p53^{WT}$ and four spectra of $p53^{PBM4}$, respectively). (**E**) Representative amide I bands of $p53^{WT}$ and $p53^{1–355}$ bound to DNA_{RE}. Spectra are normalized to the area of the amide I bands. (**F**) Difference spectrum of $p53^{WT}$ and $p53^{1–355}$ bound to DNA_{RE}. Average curve (red) and standard deviation (grey) of 16 difference spectra were calculated (combinations of four spectra of $p53^{WT}$ and four spectra of $p53^{1–355}$, respectively).

assigned to β-structures with strong intermolecular interactions (28,37,38). Probably, those changes are related to the DBD, which consists of a central β-sandwich fold. As those β-structures are more frequent in $p53^{PBM4}$ and $p53^{1–355}$, it can be assumed that the structure of the DBD is dependent on the presence of the CTD. The difference spectrum of $p53^{WT}/p53^{1–355}$ additionally showed positive difference bands at 1672 and 1654 cm^1 for $p53^{WT}$ (Figure 2F). This spectral region is indicative of β-turn, disordered and helical structures. As those structures are additionally present in the full-length protein compared to the CTD truncated variant they can be assigned to the CTD itself. Therefore, these data suggest that the intrinsically disordered CTD adopts β-turn or helical structures, when bound to DNA.

Moreover, to test the specificity of the binding of p53 to DNA we immobilized a version of the response element with a randomly scrambled base sequence (DNA_{scrRE}). The IR spectrum of the immobilized DNA_{scrRE} was almost identical to the spectrum of DNA_{RE}, verifying that only the sequence, yet not the structure of the DNA was changed (Supplementary Figure S1A). The band position at 1222 cm^{-1}, which arises by the anti symmetric phosphate vibration of the DNA backbone, is indicative of double-stranded B-form DNA as described before (34). We observed only a weak signal of the p53 amide I band upon addition to the immobilized DNA_{scrRE} (Supplementary Figure S1C), confirming that the sequence-independent binding is much weaker than the sequence-specific DNA binding. We also tested the binding of $p53^{PBM4}$ and $p53^{1–355}$ to the immobilized DNA_{scrRE}. In this case, we did not observe any p53 signal (data not shown), which is consistent with previous studies showing that the sequence-independent binding of p53 to DNA is largely mediated via the CTD (21,25,26). Interestingly, only ∼50% of $p53^{WT}$ bound to DNA_{scrRE} was removed by 'high salt washing' (Supplementary Figure S1D). This suggests that not only strong electrostatic interactions, like ionic interactions, but probably also weaker binding mechanisms, like hydrophobic interactions contribute to this binding. Due to the low signal intensity after binding of $p53^{WT}$ to DNA_{scrRE}, it was challenging to perform secondary structure analysis and the difference spectrum of $p53^{WT}$-DNA_{RE} / $p53^{WT}$-DNA_{scrRE} exhibited high standard deviation (Supplementary Figure S1E). Nevertheless, a slight, but still consistent, negative difference band at 1630 cm^{-1}, which is indicative of β-structures, was observed for $p53^{WT}$ bound to DNA_{scrRE} in comparison to DNA_{RE}. This indicates that distinct structural features are responsible for the different binding mechanisms of sequence-specific and sequence-independent DNA binding of p53.

Structural characterization and immobilization of poly(ADP-ribose)

The IR spectra of nucleic acids consist of characteristic bands, some of which can be assigned to distinct secondary structures (34). To the best of our knowledge, so far, no IR spectroscopic data of PAR has been reported. To characterize the structure of PAR and to test the previously postulated hypothesis that PAR may form secondary structures (8,9) we analyzed the spectral characteristics of PAR by ATR-FTIR spectroscopy. To this end, we compared the IR spectra of unfractionated PAR and monomeric ADP-ribose, which served as a reference, because it does not form secondary structures. Both IR spectra displayed the same characteristic bands including the antisymmetric and symmetric phosphate vibrations (1232 cm^{-1} and 1073 cm^{-1}) and typical vibrations due to the adenine (1649, 1606, 1579 and 1478 cm^{-1}) and ribose moieties (1335 cm^{-1}) (Figure 3A). The position of the antisymmetric phosphate vibration is very sensitive to the backbone conformation and therefore shows distinct positions for different secondary structures, i.e. A-form, B-form, Z-form DNA (34). PAR, as well as ADP-ribose displayed the same position of the antisymmetric phosphate vibration at 1232 cm^{-1}, which is typical for A-form DNA/RNA. Moreover, both spectra showed the same band at 1335 cm^{-1}, which is sensitive to the sugar conformation. This position is typical for adenosine with a C3′-endo ribose conformation, which can be found in various RNAs (39). Secondary structures with a C2′-endo ribose conformation, which is indicative for B-form DNA, would result in a shift from 1335 to 1344 cm^{-1} (34,39). Another band that is sensitive to secondary structure elements occurs at 1478 cm^{-1}. The position of this band would be affected by any interaction at the adenine N7 site, as it was for example observed by the formation of triple helices (34,40,41). In conclusion, no significant differences in IR spectra between PAR and ADP-ribose were observed. Therefore, PAR does probably not form secondary structures under the studied conditions.

Next, we immobilized PAR on the PEG–biotin–streptavidin modified crystal surface to study the non-covalent PAR-p53 interaction and its structural consequences via ATR-FTIR spectroscopy. For this purpose, it was necessary to modify PAR with a biotin tag. In this respect, we previously developed a method to end-label PAR via hydrazide–biotin (33). Although, in this case the label is expected to be irreversible, as the reaction is performed under reductive amination condition, we observed a loss of the biotin-label after long-term storage at −20°C. This indicates that the reductive amination is not fully efficient under the used conditions and therefore insufficient for the current application. As an alternative, we developed a novel approach by end-labeling PAR via alkoxyamine-biotin, which results in an oxime bond (Figure 3B). Previously, it was shown for a structurally simple oxime molecule to be 1000 times more stable than isostructural hydrazones (42). As the p53–PAR interaction is chain length dependent with higher affinities for longer PAR chains (2,33), we size-fractionated the biotinylated PAR via HPLC (Supplementary Figure S2). Polyacrylamide gel electrophoresis and subsequent silver staining and immunoblotting combined with the detection of the biotin label confirmed the efficient biotinylation of the individual PAR fractions (Figure 3C). To study the non-covalent PAR-p53 interaction we then immobilized three different chain lengths, i.e., a 20mer, 30mer and 50mer of PAR, on the modified ATR crystal surface. Figure 3D shows that all three PAR fractions were efficiently immobilized. The strongest signal was observed for PAR_{20mer}, followed by PAR_{30mer} and PAR_{50mer}. This is probably due to the steric hindrance of longer and probably also more branched PAR chains. The position of the antisymmetric phosphate vibration was the same for all

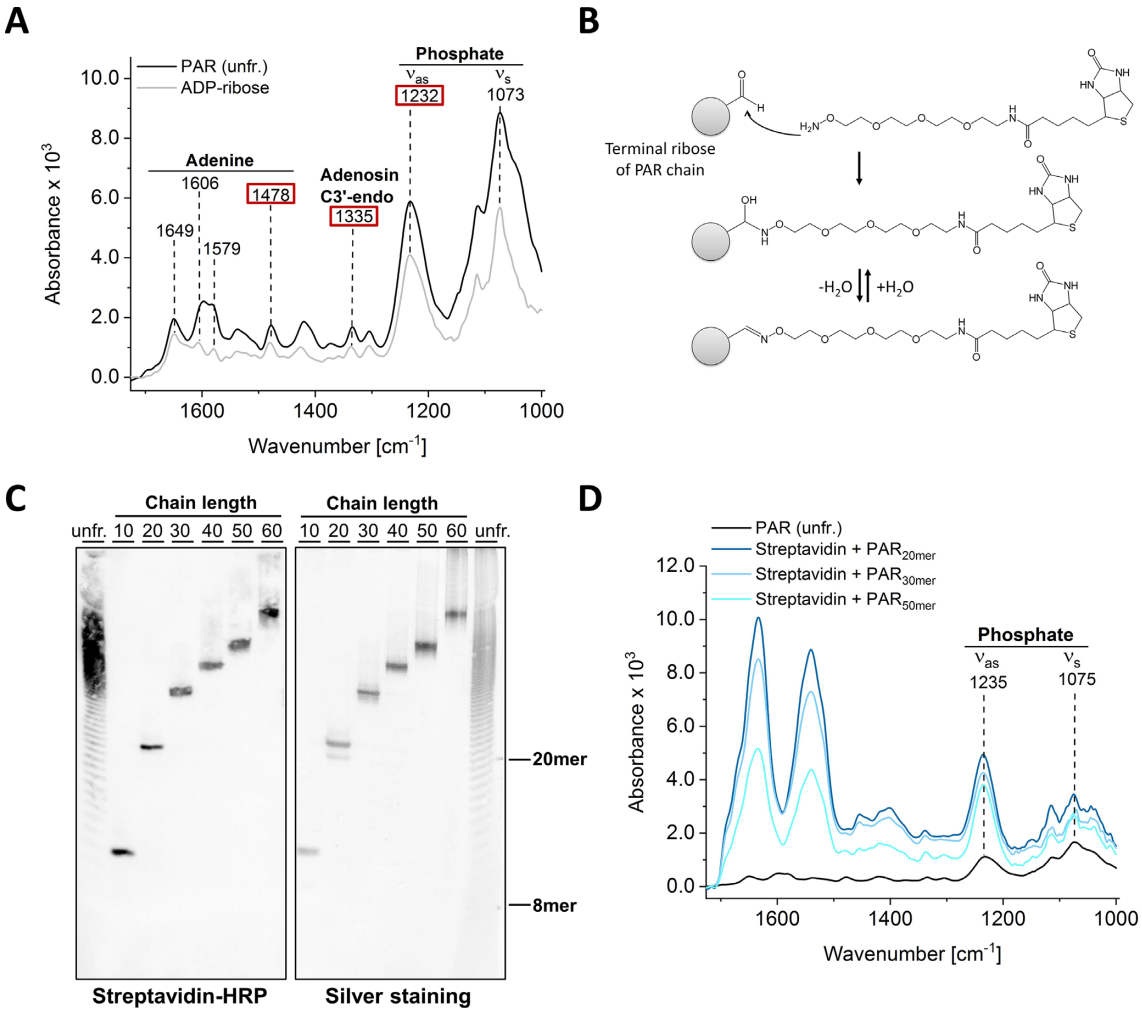

Figure 3. Spectroscopic characterization of PAR. (**A**) Comparison of the spectra of unfractionated (unfr.) PAR and ADP-ribose measured on the unmodified crystal surface for secondary structure analysis. ADP-ribose, which per se lacks the potential to form any secondary structures, served as a reference. Selected vibrational modes, sensitive to distinct secondary structures, are highlighted in red and discussed in the text. (**B**) Strategy for the end-biotinylation of PAR via oxime ligation. (**C**) Biotinylated PAR chains were separated on a 20% acrylamide gel and visualized either by blotting PAR on a membrane and detecting biotin via streptavidin-HRP (left panel) or by silver staining of the gel (right panel). (**D**) Immobilization of biotinylated PAR of different chain lengths on the PEG-biotin modified surface via streptavidin. Representative spectra of PAR in combination with streptavidin are shown. Antisymmetric (ν_{as}) and symmetric phosphate vibrations (ν_s) are highlighted.

PAR chain lengths (1232 cm^{-1}) indicating no chain-length dependent formation of secondary structures, which is in line with the comparison of the spectra of unfractionated PAR and ADP-ribose.

Structural analysis of the non-covalent p53-poly(ADP-ribose) interaction

To study the molecular mechanism of the non-covalent p53–PAR interaction and its dependence on PAR chain length we incubated $p53^{WT}$ with immobilized PAR of different chain lengths (i.e. 20mer, 30mer, 50mer). As expected, the intensity of the amide I band of $p53^{WT}$ relative to the immobilized PAR amount increased for longer PAR chains (Figure 4A). On the one hand, this might be due to the higher binding affinity of p53 to longer PAR chains (2,33). Alternatively, this might be a consequence of a higher binding capacity of longer PAR chains, resulting in binding of several p53 molecules to one long PAR chain. After exchanging the buffer on the crystal surface and thereby removing unbound and weakly bound p53 molecules, we again quantified the amount of bound p53. Interestingly, the p53 signal did not change significantly for PAR of all chain lengths upon buffer exchange (Supplementary Figure S3A). This indicates a strong interaction of $p53^{WT}$ with PAR with very low binding off-rates, in the same way as observed for the $p53^{WT}$-DNA_{RE} interaction (Supplementary Figure S1C). $p53^{WT}$ bound to PAR could be easily removed by washing the crystal with 500 mM NaCl, which suggests electrostatic interactions of PAR and p53 that can be disrupted by increasing the ionic strength. There were no major structural differences between p53 bound to PAR of different chain lengths (Supplementary Figure S3B). Still, we observed a slight increase at ~1645 cm^{-1} for longer PAR chains, suggesting a chain-length dependent increase of disordered regions within p53. Therefore, we conclude

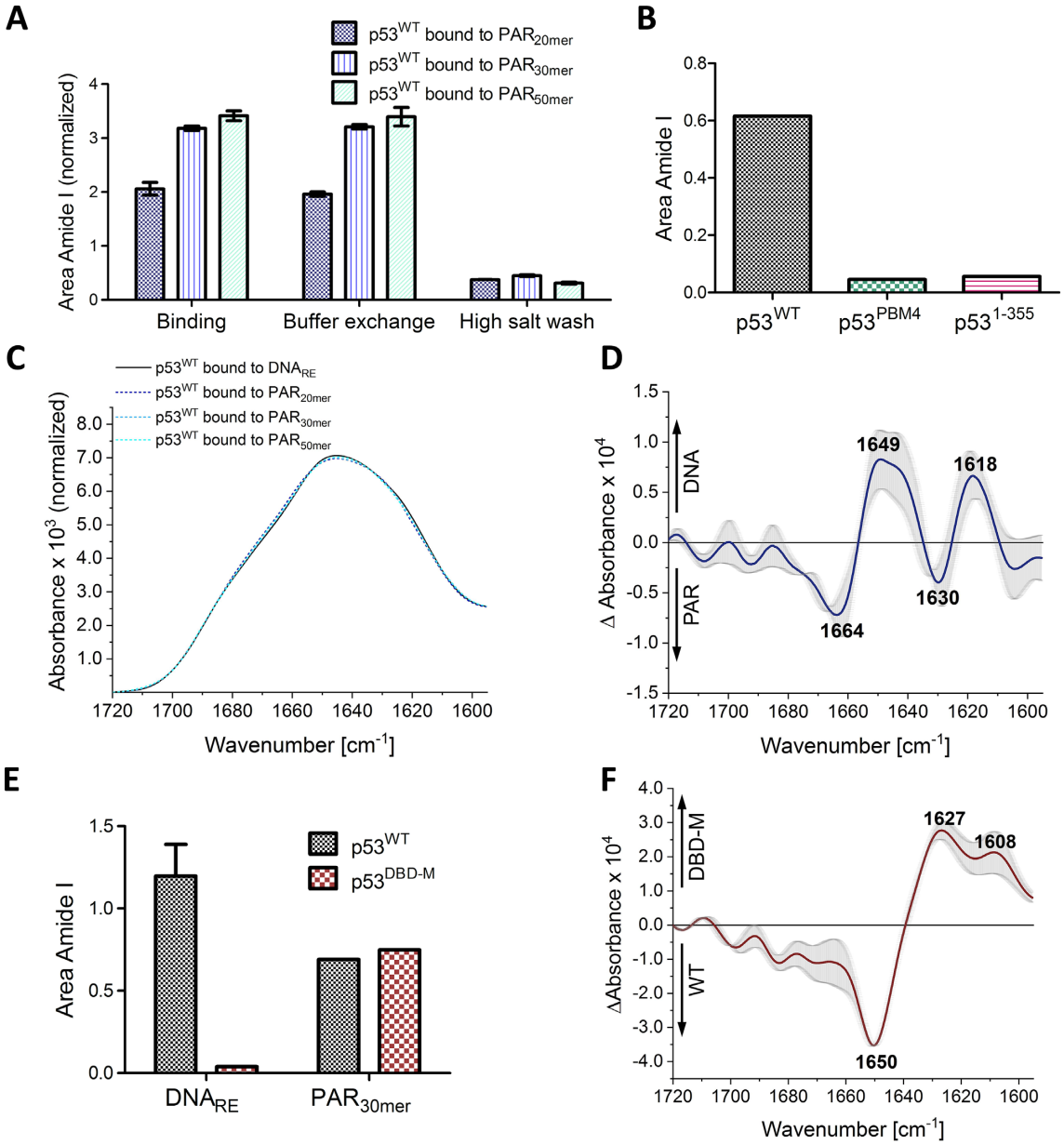

Figure 4. PAR binding is dependent on p53's CTD and results in distinct secondary structural features. (**A**) Comparison of the binding of $p53^{WT}$ to immobilized PAR of different chain lengths. First, p53 variants were added to immobilized PAR ('binding'), second, the buffer was exchanged to remove unbound protein ('buffer exchange'), and finally, the surface was washed with 500 mM NaCl to test the reversibility of the binding ('high salt wash'). Areas of the amide I bands were calculated and normalized to the immobilized PAR. (**B**) Comparison of the binding of different p53 variants to immobilized PAR_{20mer}. (**C**) Representative amide I bands of $p53^{WT}$ bound to DNA_{RE} or to PAR of different chain lengths. Spectra are normalized to the area of the amide I bands. (**D**) Difference spectrum of $p53^{WT}$ bound to DNA_{RE} and to PAR, respectively. Average curve (blue) and standard deviation (grey) from difference spectra of p53 bound to PAR_{20mer}, PAR_{30mer} or PAR_{50mer} and to DNA_{RE} were calculated (combined data from Supplementary Figure S3C). (**E**) Comparison of the binding of $p53^{WT}$ and a DNA binding domain mutant ($p53^{DBD\text{-}M}$) to DNA_{RE} and to PAR_{30mer}. (**F**) Difference spectrum of $p53^{WT}$ and $p53^{DBD\text{-}M}$ bound to PAR 30mer. Average curve (red) and standard deviation (grey) of four difference spectra was calculated (four spectra of $p53^{WT}$ and one spectrum of $p53^{DBD\text{-}M}$).

that the overall binding mechanism of p53 to PAR seems to be independent of PAR chain length, yet that small structural variations could contribute to the higher affinity of p53 to longer PAR chains. Previously, we showed that the non-covalent PAR-p53 interaction is mainly mediated via the CTD (2). Therefore, we tested the binding of the variants $p53^{PBM4}$ and $p53^{1–355}$ to immobilized PAR (Figure 4B). As expected, both p53 variants did not show any significant p53 signal, confirming the dependence of PAR binding on the CTD and especially on the positively charged aa of the CTD. Albeit, the sequence-specific DNA binding of p53 is mainly mediated via the DBD. To analyze the differences in binding mechanisms we analyzed the amide I bands of $p53^{WT}$ bound to DNA_{RE} in comparison to p53 bound to PAR. As the overall shapes of the amide I bands appeared similar, large structural differences can be excluded

(Figure 4C). However, in the difference spectra of p53–DNA_{RE}/p53–PAR distinct structural variations could be resolved (Figure 4D, Supplementary Figure S3C). Positive difference bands refer to $p53^{WT}$ bound to DNA_{RE} and negative difference bands refer to $p53^{WT}$ bound to PAR. A negative difference band was observed at 1630 cm^{-1} and a positive difference band was observed at 1618 cm^{-1}. Both bands can be assigned to β-structures. This shift to lower frequencies, i.e. 1630 $cm^{-1} \rightarrow$ 1618 cm^{-1}, can be a result of stronger hydrogen bonds and an increase in the number of β-strands (28,37,38). It was described previously via a multi-technique approach including small angle X-ray scattering, electron microscopy and NMR spectroscopy that DNA binding can result in the compaction of p53 (18). Such a compaction could lead to an increased coupling between the different β-sheets, explaining the observed band shift to lower frequencies of $p53^{WT}$ bound to DNA compared to $p53^{WT}$ bound to PAR. Moreover, a clear positive difference band was observed at 1649 cm^{-1}, which can be assigned to α-helical or disordered structures, and a clear negative band was observed at 1664 cm^{-1}, which can be assigned to 3_{10}-helical or also β-turn structures. Thus, these data provide evidence that additional structural changes within $p53^{WT}$ occur upon binding to DNA and PAR.

To analyze the role of the DBD with regard to DNA and PAR binding, we tested a p53 variant harboring several mutations within the DBD ($p53^{DBD\text{-}M}$) that are known to be important for sequence-specific DNA binding and the correct folding of the DBD. $p53^{DBD\text{-}M}$ did not bind to immobilized DNA_{RE}, which proofed that the inserted mutations disturb the DBD–DNA interaction (Figure 4E). In contrast, binding of $p53^{DBD\text{-}M}$ to immobilized PAR occurred at a similar level as compared to $p53^{WT}$ (Figure 4E). Analysis of the difference spectra of $p53^{DBD\text{-}M}$/$p53^{WT}$ showed a strong negative band at 1650 cm^{-1} and strong positive bands at 1627 and 1608 cm^{-1} for $p53^{DBD\text{-}M}$ compared to $p53^{WT}$ (Figure 4F). Those band positions are characteristic for disordered or α-helical structures and β-sheets, respectively. The low frequency component at 1608 cm^{-1} is indicative of β-structured aggregates (30), suggesting that the inserted mutations resulted in the loss of disordered or α-helical structures and in the formation of aggregates. Therefore, we conclude that PAR binding is mainly dependent on the presence of the CTD rather than on a correct folding of the full-length protein.

Competitive binding of DNA and PAR to p53

Several studies revealed a correlation of transcriptional regulation and non-covalent PAR binding or covalent PARylation of p53 (2,43–45). However, the direct interplay of PAR and DNA binding on the molecular level is only poorly understood. Via electrophoretic mobility shift assays (EMSAs) it was reported that non-covalent PAR binding inhibits the sequence-specific DNA binding of p53 (2,46). However, EMSAs have several limitations, as samples are not at chemical equilibrium during electrophoresis and as some complexes are significantly more stable in the gel than in free solution (47). Our ATR-FTIR spectroscopic approach overcomes those limitations and therefore allows a direct examination of the interplay of PAR and DNA binding of p53 under buffer conditions similar to a physiological environment (i.e. 50 mM Tris, pH 7.4, 150 mM NaCl). To this end, we immobilized the DNA_{RE} substrate, allowed the p53 variants to bind, and removed unbound protein by buffer exchange. Then, we added unfractionated PAR and analyzed the intensity of the amide I band of the p53 spectra over time. Remarkably, the signal of $p53^{WT}$ decreased rapidly upon the addition of PAR (Figure 5A and D). This indicates that $p53^{WT}$ preferentially binds to PAR as compared to DNA. PAR was not detectable in the IR spectra suggesting that PAR itself was not significantly enriched at the crystal surface. Thus, even though both binding partners have distinct binding domains within the p53 protein, this finding points to an exclusive binding of p53 either to DNA or to PAR, but not both at the same time. Furthermore, these results suggest a strong electrostatic attraction of $p53^{WT}$ to PAR, which can disrupt the sequence-dependent p53–DNA binding. Also, it is conceivable that the p53–PAR interaction immediately induces structural changes within p53 which abolishes its sequence-specific DNA binding via the DBD and release of the p53–PAR complex from the crystal surface. As expected, the DNA binding of $p53^{1–355}$ and $p53^{PBM4}$, which are deficient in PAR binding, was not influenced by the presence of PAR (Figure 5B–D). The slight decrease of the signal of the p53 variants was independent of the presence of PAR (Supplementary Figure S1B). Vice versa, we also tested the competitive effect of PAR and DNA binding to p53 by immobilizing PAR on the surface and subsequently adding DNA to the supernatant. In this case, the signal of $p53^{WT}$ decreased only by ∼20%, confirming a preferential binding of p53 to PAR (Supplementary Figure S4A). We also tested the effect of PAR on the sequence-independent DNA binding of p53. As expected, in this case, the competitive effect of PAR was even more pronounced, since the sequence-independent DNA binding of p53 is much weaker compared to its sequence-specific binding (Supplementary Figure S4B). In summary, we demonstrate in a time-dependent manner and with near-physiological buffer conditions that PAR is a very efficient competitor of sequence-specific as well as sequence-independent DNA binding of $p53^{WT}$.

Impact of the CTD on the aggregation properties of p53 upon PAR and DNA binding

The core domain of p53 is of low intrinsic stability and was shown to unfold rapidly at body-temperature with a half-life of 9 min (48–50). This suggests that different binding partners can lead to a stabilizing effect of p53 in cells. Previous studies showed that the sequence-specific binding of the p53 core domain to its DNA response element leads to a stabilizing effect in terms of thermal denaturation (48). Recently, we have demonstrated by differential scanning fluorimetry (DSF) that this also holds true for full-length p53 and moreover, that PAR slightly increases the thermal stability of p53 (2). As our ATR-FTIR spectroscopic data suggest different binding mechanisms for DNA and PAR binding, we investigated the molecular mechanisms behind these observations. For this purpose, we performed temperature-induced melting experiments via CD spectroscopy providing insights into the temperature-dependent changes of sec-

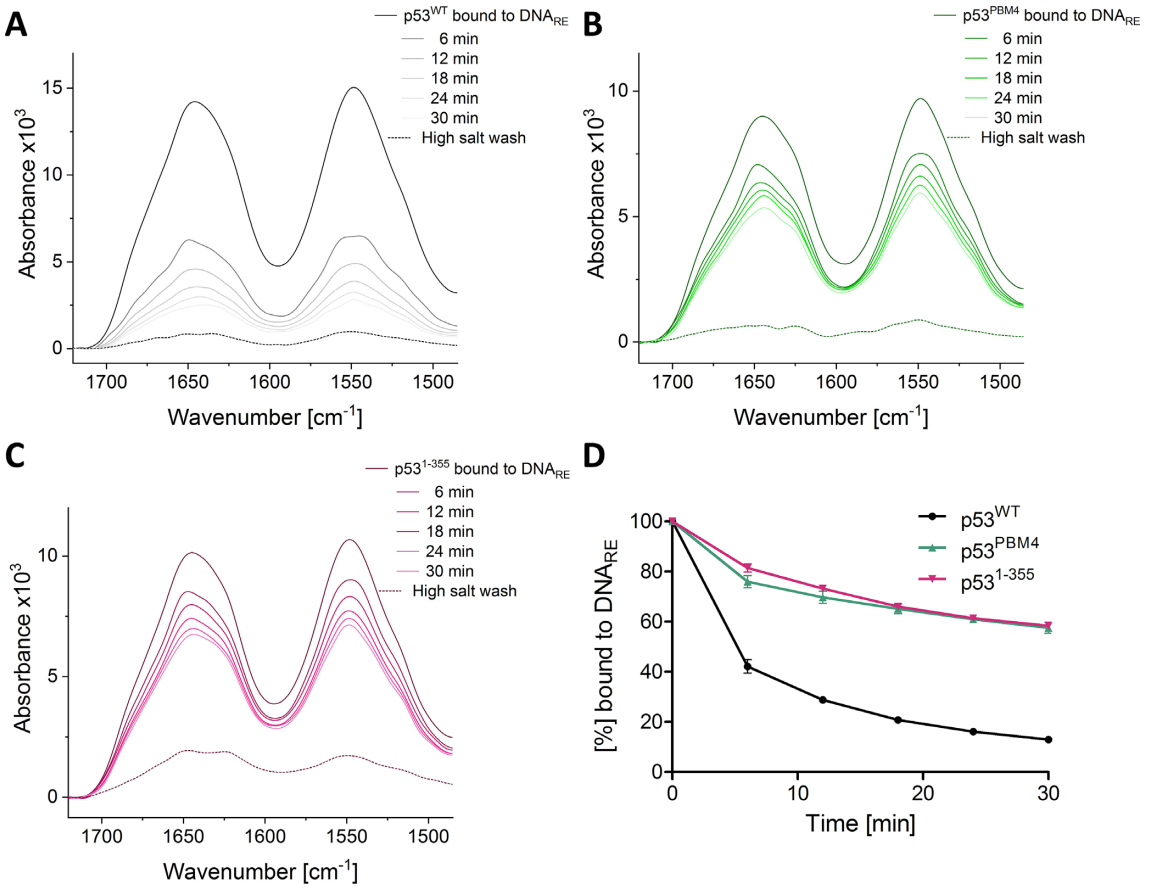

Figure 5. Competitive binding of p53 to DNA and PAR. Unfractionated PAR (100 μM, concentration in ADP-ribose units) was added to p53, which was bound to immobilized DNA_{RE}. Spectral changes were recorded over time. $p53^{WT}$ (**A**), $p53^{PBM4}$ (**B**) and $p53^{1–355}$ (**C**). (**D**) Quantitation of signal reduction by calculating the area of the amide I band. Spectra before addition of PAR were set to 100% and spectra after washing the crystal with 500 mM NaCl were set to 0%.

ondary structure of PAR, DNA and p53. To obtain comparable data we used the same buffer conditions as in our IR studies and in previous DSF experiments. Thus, due to the strong absorbance of chloride ions at low wavelengths, spectra could only be analyzed at wavelengths higher than 200 nm, allowing only qualitative analysis. The CD spectrum of DNA_{RE} at 20°C showed a minimum around 250 nm and a maximum around 270 nm, which is indicative for B-form DNA (51) (Supplementary Figure S5A). The transition temperature of 78°C was consistent with the calculated melting temperature of 79°C. The spectrum of PAR showed two minima at 220 and 270 nm, which are comparable to spectra of adenosine monophosphate (52–54), and which did not change within the studied temperature range (Supplementary Figure S5B). On the one hand, this is consistent with our IR data, indicating the absence of temperature-dependent secondary structures of PAR under the studied conditions. On the other hand, this is contradictory to previous CD spectroscopic data suggesting an α-helical structure of PAR, which is affected by temperature (8,9). However, the latter postulated secondary structures were observed at high ionic strengths (1–5 M NaCl) and below 25°C (8,9) and have so far not been described at physiological conditions. In our CD analyses, the structure of $p53^{WT}$ was stable up to 40°C, which was followed by a sudden decrease of ellipticity (Figure 6A and B). This decrease of ellipticity is probably due to the fast and irreversible formation of insoluble aggregates, which were visible after the experiment and which cannot be analyzed by CD spectroscopy due to scattering effects. This is supported by the simultaneous increase of the high tension (HT) signal, which indicates a decrease of light intensity reaching the detector (Supplementary Figure S5C). This decrease can be caused by scattering of insoluble aggregates. The thermal denaturation of $p53^{WT}$ in the presence of DNA_{RE} looked similar but was shifted ∼5°C toward higher temperatures (Figure 6A and B, Supplementary Figure S5C). This stabilizing effect is in line with our previous DSF experiments (2). Notably, the DNA signal did not change upon aggregation of p53 indicating that the p53–DNA interaction was disrupted in a first step, and p53 formed aggregates in a second step. Interestingly, not the melting temperature itself, but the characteristics of thermal denaturation of p53 were strongly influenced by the presence of PAR (Figure 6A and B). Instead of a sudden decrease in ellipticity at 40°C, the presence of PAR resulted first in an increase at 220 nm, followed by a slow decrease. This behaviour was also observed for $p53^{PBM4}$ and $p53^{1–355}$, yet even in the absence of PAR, indicating a structural regulation via the CTD (Figure 6B and Supplementary Figure SD–G). The decrease

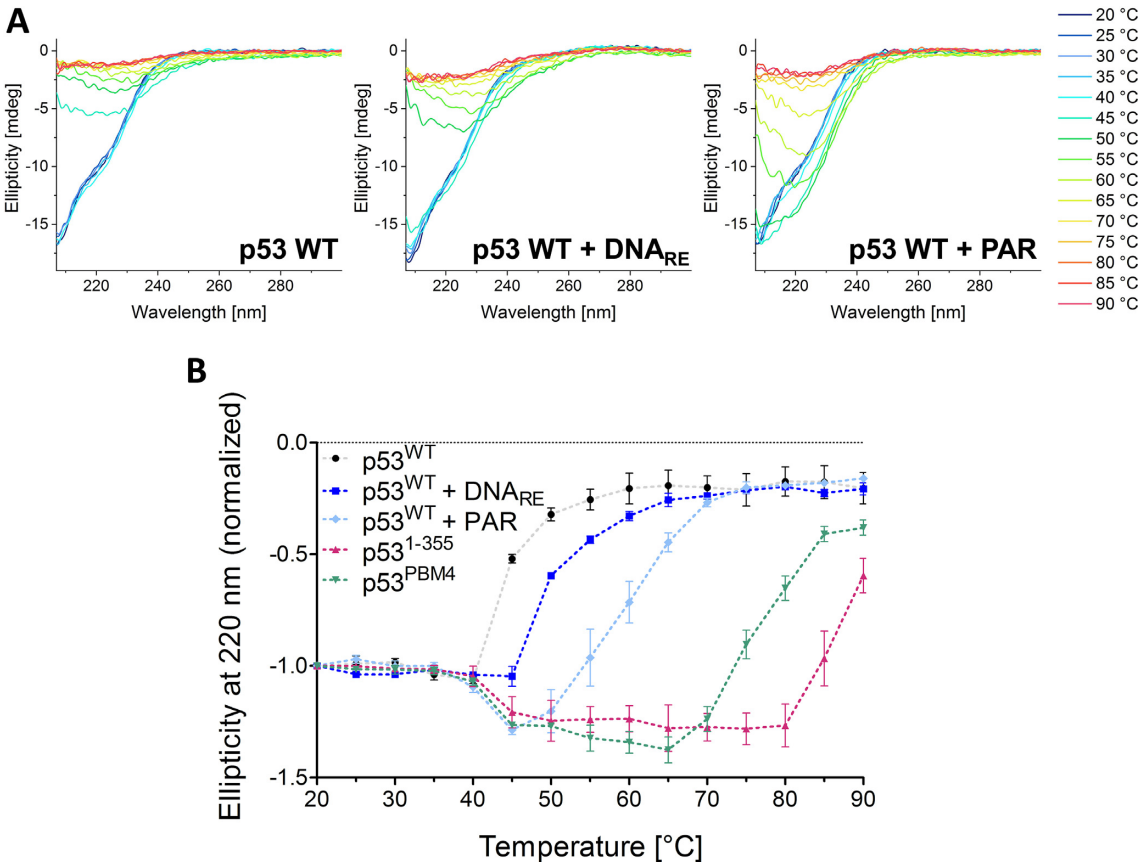

Figure 6. Impact of DNA and PAR binding on the thermal stability of p53 variants studied by CD spectroscopy. (**A**) Representative spectra of the thermal denaturation of $p53^{WT}$ in the absence or presence of DNA_{RE} or unfractionated PAR. (**B**) Ellipticity at 220 nm of p53 variants in the absence or presence of DNA_{RE} or unfractionated PAR plotted against temperature and normalized to ellipticity at 20°C. Representative spectra of $p53^{PBM4}$ and $p53^{1–355}$ are shown in Supplementary Figure S5D and E.

of ellipticity can again be assigned to the formation of insoluble aggregates as it correlates with an increase of the HT signal (Supplementary Figure S5C).An increase at 220 nm has already been observed in other protein studies and was mostly assigned to the formation of β-structured aggregates and amyloid-like fibrils (55–57). Several studies postulated a tendency of the core domain and of the tetramerization domain of p53 to form amyloid like structures (58–60). However, to our knowledge so far, the role of the CTD in these processes has not been analyzed. Due to the fact that the insoluble material could not be analyzed via CD spectroscopy and therefore we do not have information on its secondary structure, we cannot conclude if changes in the CTD induce the formation of β-structured aggregates or if those changes just lead to the stabilization of their solubility. Comparable to DNA_{RE}, the signal intensity of PAR did not change upon formation of insoluble aggregates, indicating that the p53–PAR interaction is disrupted before p53 precipitates. We also tested the effect of DNA and PAR on the thermal stability of the variants $p53^{PBM4}$ and $p53^{1–355}$ (Supplementary Figure S5D–G). Comparable to $p53^{WT}$, DNA showed a stabilizing effect. As expected, PAR did not have a significant impact on the thermal denaturation. Comparing the binding of p53 to DNA and PAR, we conclude that only DNA binding has a pronounced effect on the thermal stability of p53. Yet, binding to PAR is probably more heat resistant, thus shifting the formation of irreversible and insoluble aggregates to higher temperatures. This supports our findings that PAR and DNA binding work via different mechanisms with distinct structural consequences.

DISCUSSION

Almost 70% of all DNA-binding proteins have disordered terminal regions lacking a globular regular fold (61). Those intrinsically disordered regions (IDRs) often possess key regulatory functions. For example, IDRs can facilitate diffusion of proteins along DNA or can regulate the transition from a non-specific to a specific DNA-protein complex (62,63). Due to the high flexibility of IDRs, current structural data of DNA-binding proteins mainly lack information on those domains. Here, we provide structural information on the tumour suppressor protein p53, which represents a typical DNA-binding protein with a regulatory intrinsically disordered C-terminal domain. Although NMR studies on isolated CTD peptides have been performed (19–21), the transferability of such results to the full-length protein remains elusive. Our ATR-FTIR spectroscopic approach allows structural studies of full-length p53, as it is not limited to the size and flexibility of the molecule of interest. Moreover, this method is extremely powerful with re-

gards to subtle structural changes within proteins and provides access to the dynamic conformational changes of proteins under near-physiological conditions. Moreover, we obtained structural information in the low micromolar range (5 μM), which allows to examine the conformation and conformational changes of proteins with the propensity to form aggregates at high concentrations.

In the current study, we analyzed in detail the molecular mechanisms behind the interplay of DNA and PAR binding to p53. We demonstrate that the CTD represents the central regulator of sequence-specific and sequence-independent DNA and PAR binding (Figure 7). Although sequence-specific DNA binding and PAR binding both show high binding strengths with very low binding off-rates, PAR represents the preferred binding partner and can very efficiently abrogate DNA binding. This regulation is probably mainly driven by electrostatic attractions between the positively charged CTD and the highly negatively charged PAR polymer, as PAR binding was almost completely reversible at high ionic strengths. Moreover, we observed distinct structural changes of p53 binding to DNA and to PAR, respectively, which could additionally stabilize and thereby favour PAR binding. Recently, it was shown that PAR can serve as a trigger for liquid-liquid demixing in cells, which is mainly driven by electrostatic interactions and which results in the rapid assembly of various intrinsically disordered domains at DNA strand breaks (64). As several studies revealed a correlation of transcriptional regulation of p53 and PARylation (2,45,65,66), PAR-dependent liquid demixing processes might also be involved in the regulation of p53. It is plausible that cells have developed strong triggers like the swift and dynamic formation of the highly negatively charged PAR polymer to efficiently control p53's DNA binding to its >4,000 binding sequences within the human genome.

Up to date, no structural information of the CTD in context of full-length p53 exists. By comparing the amide I bands of full length $p53^{WT}$ and the CTD truncated variant $p53^{1–355}$ both bound to DNA, we could draw conclusions about the structure of the CTD. Besides disordered structures, our data suggest β-turn or helical structures of the CTD. Those assumptions are supported by previous MD simulations of CTD peptides suggesting the occurrence of both structures (22). Furthermore, this hypothesis is strengthened by previous NMR studies proposing local helix formations of CTD peptides bound to DNA (21). A key role of the CTD in the regulation of sequence-specific DNA binding is well established and here we could confirm recent data showing a positive regulatory function (25–27,67). Still, the mechanism and structural consequences behind this regulation remain controversial. Two major hypotheses exist, which are not mutually exclusive. Thus, on the one hand, the CTD may simply act as an anchor, which stabilizes the DNA–p53 complex via several non-specific interactions. On the other hand, it is possible that the CTD induces conformational changes within the p53 tetramer upon binding and thereby stabilizes the p53–DNA complex. The latter is also known as the so-called 'induced-fit theory'. Although two studies support this theory (27,68), so far, direct evidence is missing. By comparing the IR spectra of $p53^{WT}$ and CTD mutants bound to DNA, we can exclude major structural changes caused by the CTD. Yet, the decrease of secondary structure components at ∼1625 cm^{-1} in $p53^{WT}$ compared to the CTD mutants indicates a decrease of β-sheets and therefore small but distinct structural changes caused by the CTD. This suggests a reduction of β-sheets induced by the binding of the CTD to DNA. To confirm this hypothesis IR data of p53 in the absence of DNA would be expedient. However, since p53 functions as a homotetramer, site-specific immobilization of p53 via one monomer remains an unsolved task and so far, all attempts to immobilize p53 on the crystal surface resulted in the loss of its functionality.

The 'induced-fit theory' was not only suggested for the CTD, but also for the isolated DBD. Crystal structures of the DBD in the absence or presence of DNA revealed rearrangements of the L1 loop stabilizing the DBD-DNA interaction and thereby strongly affecting binding off-rates (69,70). In the present study, we revealed that DNA binding off-rates of full-length p53 were mainly influenced by the CTD. While $p53^{WT}$ bound to DNA showed very low binding off-rates, both CTD mutants showed a 25% higher release from DNA compared to $p53^{WT}$. This suggests that in context of the full-length protein, the observed independent structural rearrangements within the DBD only slightly affect DNA binding, whereas the CTD strongly stabilizes the p53–DNA interaction.

Our data provide strong evidence for two distinct binding modes of p53 to DNA and PAR: On the one hand, the CTD-mediated binding including sequence-independent DNA and PAR binding, and, on the other hand, the DBD-mediated binding including sequence-specific DNA binding (Figure 7). Interestingly, p53 bound to DNA_{scrRE} showed similar effects on the secondary structure as p53 bound to PAR, suggesting similar binding mechanisms driven by the CTD. In contrast, the binding mechanism observed for sequence-specific DNA binding resulted in distinct secondary structures. The band characteristic for β-sheets shifted to lower frequencies (∼ 1618 cm^{-1}) indicates a compaction of the β-sheet-rich DBDs. Previous high resolution crystal structures of the p53 DBD core domain in the presence of DNA revealed a self-assembly of DBD domains driven by protein-protein interactions even in the absence of the tetramerization domain (71). This process of compaction upon DNA binding could later be confirmed for the full-length protein using a combination of small angle X-ray scattering, electron microscopy and NMR spectroscopy (18,72). Additionally, we observed positive difference bands at 1649 cm^{-1} for the DBD-driven sequence-specific DNA interaction and negative difference bands at 1664 cm^{-1} for the CTD-driven PAR interaction indicating distinct and potentially very dynamic structural changes for the different interaction partners. To date, such structural changes of p53 upon binding to macromolecules have not been reported and are therefore probably caused by the so far structural inaccessible disordered domains within the full-length protein. Thus, we provide further evidence that dependent on the binding partner the disordered domains of p53 can adopt distinct secondary structures.

p53 is the most frequently mutated gene in human cancer. Most of the mutations are missense mutations and disturb the DBD. Besides a loss of function due to the inserted mu-

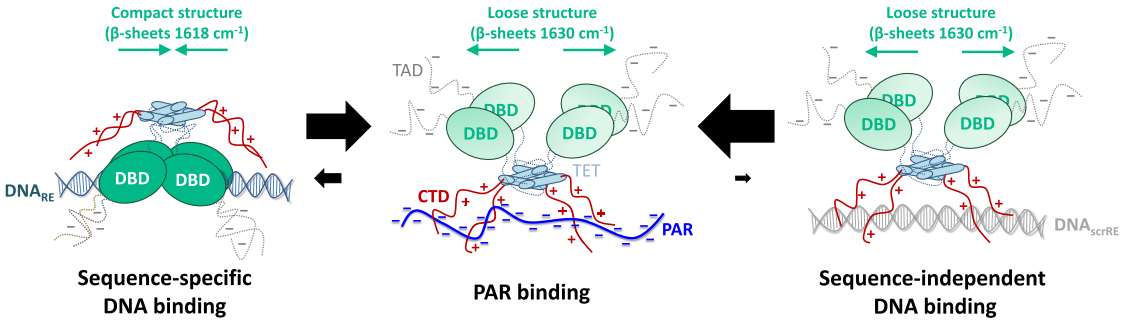

Figure 7. Mechanistic model for the interplay of DNA and PAR binding to p53. The intrinsically disordered C-terminal domain (CTD) of p53 functions as a central regulator of DNA and PAR binding. Electrostatic attractions between the positively charged CTD and the negatively charged PAR and DNA backbone combined with distinct structural rearrangements of p53 determine binding strength. Thus, the highly negatively charged PAR represents the preferred binding partner of p53. In the CTD-driven interactions with PAR and DNA_{scrRE} (i.e. sequence-independent DNA binding), the DBD remains a loose structure indicated by the band position of β-sheets at ∼1630 cm^{-1} within the infrared spectrum. In contrast, sequence-specific DNA binding to the DNA_{RE} substrate is mainly mediated via the DBD resulting in a compaction of the β-sheet-rich structure indicated by a shift of the band position of β-sheets to ∼1618 cm^{-1}.

tations previous studies showed that mutated p53 can gain new functions promoting tumorigenesis, the so-called gain-of-function mutants (GOF) (73,74). Here, we analyzed a p53 mutant harbouring several point mutations within the DBD. We observed that even though the overall structure was disturbed, and sequence-specific DNA binding was abrogated, PAR binding was not affected. The interplay of cancer-associated mutant p53 and PARylation has so far not been addressed and might reveal new aspects of GOF regulation with potential applications for cancer therapy.

SUPPLEMENTARY DATA

Supplementary Data are available at NAR Online.

ACKNOWLEDGEMENTS

We thank Katharina Hilger and Nicolai Wagner for their contributions during the initiating phase of this project. Further, we thank Katharina Henke for support during the development of the ATR-FTIR spectroscopic approach.
Authors contributions: Conceptualization and data interpretation, A.K., A.B., K.H., AM; experimental research and data analysis, A.K., A.S., A.F.; writing – original draft, A.K.; writing - review and editing, A.K., A.S., A.F., A.B., K.H., A.M.; supervision, project administration and funding acquisition, A.B., K.H., A.M.

FUNDING

German Research Foundation (DFG) through the Konstanz Research School Chemical Biology (KoRS-CB, GSC 218); Collaborative Research Center 969 (CRC969, projects A02 and B04); Collaborative Research Center 1214 (CRC1214, project A03); grant MA4905/4-1; *Zukunftskolleg* of the University of Konstanz. Funding for open access charge: CRC969, University of Konstanz.
Conflict of interest statement. None declared.

REFERENCES

1. Jackson,S.P. and Bartek,J. (2009) The DNA-damage response in human biology and disease. *Nature*, **461**, 1071.
2. Fischbach,A., Kruger,A., Hampp,S., Assmann,G., Rank,L., Hufnagel,M., Stockl,M.T., Fischer,J.M.F., Veith,S., Rossatti,P. *et al.* (2018) The C-terminal domain of p53 orchestrates the interplay between non-covalent and covalent poly(ADP-ribosyl)ation of p53 by PARP1. *Nucleic Acids Res.*, **46**, 804–822.
3. Laptenko,O., Tong,D.R., Manfredi,J. and Prives,C. (2016) The tail that wags the dog: How the disordered C-Terminal domain controls the transcriptional activities of the p53 Tumor-Suppressor protein. *Trends Biochem. Sci.*, **41**, 1022–1034.
4. Langelier,M.F., Eisemann,T., Riccio,A.A. and Pascal,J.M. (2018) PARP family enzymes: regulation and catalysis of the poly(ADP-ribose) posttranslational modification. *Curr. Opin. Struct. Biol.*, **53**, 187–198.
5. Ray Chaudhuri,A. and Nussenzweig,A. (2017) The multifaceted roles of PARP1 in DNA repair and chromatin remodelling. *Nat. Rev. Mol. Cell Biol.*, **18**, 610–621.
6. Hottiger,M.O., Hassa,P.O., Luscher,B., Schuler,H. and Koch-Nolte,F. (2010) Toward a unified nomenclature for mammalian ADP-ribosyltransferases. *Trends Biochem. Sci.*, **35**, 208–219.
7. Hayashi,K., Tanaka,M., Shimada,T., Miwa,M. and Sugimura,T. (1983) Size and shape of poly(ADP-ribose): Examination by gel filtration, gel electrophoresis and electron microscopy. *Biochem. Biophys. Res. Commun.*, **112**, 102–107.
8. Minaga,T. and Kun,E. (1983) Spectral analysis of the conformation of polyadenosine diphosphoribose. Evidence indicating secondary structure. *J. Biol. Chem.*, **258**, 725–730.
9. Minaga,T. and Kun,E. (1983) Probable helical conformation of poly(ADP-ribose). The effect of cations on spectral properties. *J. Biol. Chem.*, **258**, 5726–5730.
10. Schultheisz,H.L., Szymczyna,B.R. and Williamson,J.R. (2009) Enzymatic synthesis and structural characterization of 13C, 15N-Poly(ADP-ribose). *J. Am. Chem. Soc.*, **131**, 14571–14578.
11. Teloni,F. and Altmeyer,M. (2015) Readers of poly(ADP-ribose): designed to be fit for purpose. *Nucleic Acids Res.*, **44**, 993–1006.
12. Pleschke,J.M., Kleczkowska,H.E., Strohm,M. and Althaus,F.R. (2000) Poly(ADP-ribose) binds to specific domains in DNA damage checkpoint proteins. *J. Biol. Chem.*, **275**, 40974–40980.
13. Kastenhuber,E.R. and Lowe,S.W. (2017) Putting p53 in context. *Cell*, **170**, 1062–1078.
14. Wei,C.L., Wu,Q., Vega,V.B., Chiu,K.P., Ng,P., Zhang,T., Shahab,A., Yong,H.C., Fu,Y., Weng,Z. *et al.* (2006) A global map of p53 transcription-factor binding sites in the human genome. *Cell*, **124**, 207–219.
15. Clore,G.M., Ernst,J., Clubb,R., Omichinski,J.G., Kennedy,W.M., Sakaguchi,K., Appella,E. and Gronenborn,A.M. (1995) Refined solution structure of the oligomerization domain of the tumour suppressor p53. *Nat. Struct. Biol.*, **2**, 321–333.
16. Joerger,A.C. and Fersht,A.R. (2008) Structural biology of the tumor suppressor p53. *Annu. Rev. Biochem.*, **77**, 557–582.

17. Cho,Y., Gorina,S., Jeffrey,P.D. and Pavletich,N.P. (1994) Crystal structure of a p53 tumor suppressor-DNA complex: understanding tumorigenic mutations. *Science*, **265**, 346–355.
18. Tidow,H., Melero,R., Mylonas,E., Freund,S.M.V., Grossmann,J.G., Carazo,J.M., Svergun,D.I., Valle,M. and Fersht,A.R. (2007) Quaternary structures of tumor suppressor p53 and a specific p53–DNA complex. *Proc. Natl. Acad. Sci. U.S.A.*, **104**, 12324–12329.
19. Rust,R.R., Baldisseri,D.M. and Weber,D.J. (2000) Structure of the negative regulatory domain of p53 bound to S100B([beta][beta]). *Nat. Struct. Mol. Biol.*, **7**, 570–574.
20. Mujtaba,S., He,Y., Zeng,L., Yan,S., Plotnikova,O., Sachchidanand,Sanchez, R., Zeleznik-Le,N.J., Ronai,Z.e. and Zhou,M.-M. (2004) Structural mechanism of the bromodomain of the coactivator CBP in p53 transcriptional activation. *Mol. Cell*, **13**, 251–263.
21. Friedler,A., Veprintsev,D.B., Freund,S.M.V., von Glos,K.I. and Fersht,A.R. (2005) Modulation of binding of DNA to the C-Terminal domain of p53 by acetylation. *Structure*, **13**, 629–636.
22. Fadda,E. and Nixon,M.G. (2017) The transient manifold structure of the p53 extreme C-terminal domain: insight into disorder, recognition, and binding promiscuity by molecular dynamics simulations. *PCCP*, **19**, 21287–21296.
23. Sullivan,K.D., Galbraith,M.D., Andrysik,Z. and Espinosa,J.M. (2018) Mechanisms of transcriptional regulation by p53. *Cell Death Differ.*, **25**, 133–143.
24. Hupp,T.R. and Lane,D.P. (1994) Allosteric activation of latent p53 tetramers. *Curr. Biol.: CB*, **4**, 865–875.
25. McKinney,K., Mattia,M., Gottifredi,V. and Prives,C. (2004) p53 linear diffusion along DNA requires its C terminus. *Mol. Cell*, **16**, 413–424.
26. Tafvizi,A., Huang,F., Fersht,A.R., Mirny,L.A. and van Oijen,A.M. (2011) A single-molecule characterization of p53 search on DNA. *PNAS*, **108**, 563–568.
27. Laptenko,O., Shiff,I., Freed-Pastor,W., Zupnick,A., Mattia,M., Freulich,E., Shamir,I., Kadouri,N., Kahan,T., Manfredi,J. *et al.* (2015) The p53 C terminus controls Site-Specific DNA binding and promotes structural changes within the central DNA binding domain. *Mol. Cell*, **57**, 1034–1046.
28. Barth,A. (2007) Infrared spectroscopy of proteins. *Biochim. Biophys. Acta (BBA) - Bioenergetics*, **1767**, 1073–1101.
29. Yang,H., Yang,S., Kong,J., Dong,A. and Yu,S. (2015) Obtaining information about protein secondary structures in aqueous solution using Fourier transform IR spectroscopy. *Nat. Protoc.*, **10**, 382–396.
30. Sarroukh,R., Goormaghtigh,E., Ruysschaert,J.-M. and Raussens,V. (2013) ATR-FTIR: A "rejuvenated" tool to investigate amyloid proteins. *Biochim. Biophys. Acta (BBA) - Biomembranes*, **1828**, 2328–2338.
31. Krüger,A., Bürkle,A., Mangerich,A. and Hauser,K. (2018) A combined approach of surface passivation and specific immobilization to study biomolecules by ATR-FTIR spectroscopy. *Biomed. Spectrosc. Imaging*, **7**, 25–33.
32. Langelier,M.F., Planck,J.L., Servent,K.M. and Pascal,J.M. (2011) Purification of human PARP-1 and PARP-1 domains from Escherichia coli for structural and biochemical analysis. *Methods Mol. Biol.*, **780**, 209–226.
33. Fahrer,J., Kranaster,R., Altmeyer,M., Marx,A. and Bürkle,A. (2007) Quantitative analysis of the binding affinity of poly(ADP-ribose) to specific binding proteins as a function of chain length. *Nucleic Acids Res.*, **35**, e143.
34. Banyay,M., Sarkar,M. and Gräslund,A. (2003) A library of IR bands of nucleic acids in solution. *Biophys. Chem.*, **104**, 477–488.
35. Espinosa,J.M. and Emerson,B.M. (2001) Transcriptional regulation by p53 through intrinsic DNA/Chromatin binding and Site-Directed cofactor recruitment. *Mol. Cell*, **8**, 57–69.
36. Jawurek,M., Dröden,J., Peter,B., Glaubitz,C. and Hauser,K. (2018) Lipid-induced dynamics of photoreceptors monitored by time-resolved step-scan FTIR spectroscopy. *Chem. Phys.*, **512**, 53–61.
37. Chirgadze,Y.N. and Nevskaya,N.A. (1976) Infrared spectra and resonance interaction of amide-I vibration of the antiparallel-chain pleated sheet. *Biopolymers*, **15**, 607–625.
38. Krimm,S. and Bandekar,J. (1986) In: Anfinsen,CB, Edsall,JT and Richards,FM (eds). *Advances in Protein Chemistry*. Academic Press, Vol. **38**, pp. 181–364.
39. Liquier,J., Akhebat,A., Taillandier,E., Ceolin,F., Dinh,T.H. and Igolen,J. (1991) Characterization by FTIR spectroscopy of the oligoribonucleotide duplexes r(A-U)6 and r(A-U)8. *Spectrochim. Acta Part A: Mol. Spectrosc.*, **47**, 177–186.
40. Lindqvist,M., Sarkar,M., Winqvist,A., Rozners,E., Stromberg,R. and Graslund,A. (2000) Optical spectroscopic study of the effects of a single deoxyribose substitution in a ribose backbone: implications in RNA-RNA interaction. *Biochemistry*, **39**, 1693–1701.
41. Dagneaux,C., Liquier,J. and Taillandier,E. (1995) Sugar conformations in DNA and RNA-DNA triple helices determined by FTIR spectroscopy: role of backbone composition. *Biochemistry*, **34**, 16618–16623.
42. Kalia,J. and Raines,R.T. (2008) Hydrolytic stability of hydrazones and oximes. *Angew. Chem. (Int. Ed. Engl.)*, **47**, 7523–7526.
43. Simbulan-Rosenthal,C.M., Rosenthal,D.S., Luo,R. and Smulson,M.E. (1999) Poly(ADP-ribosyl)ation of p53 during apoptosis in human osteosarcoma cells. *Cancer Res.*, **59**, 2190–2194.
44. Lee,M.H., Na,H., Kim,E.J., Lee,H.W. and Lee,M.O. (2012) Poly(ADP-ribosyl)ation of p53 induces gene-specific transcriptional repression of MTA1. *Oncogene*, **31**, 5099–5107.
45. Wieler,S., Gagne,J.P., Vaziri,H., Poirier,G.G. and Benchimol,S. (2003) Poly(ADP-ribose) polymerase-1 is a positive regulator of the p53-mediated G1 arrest response following ionizing radiation. *J. Biol. Chem.*, **278**, 18914–18921.
46. Malanga,M., Pleschke,J.M., Kleczkowska,H.E. and Althaus,F.R. (1998) Poly(ADP-ribose) binds to specific domains of p53 and alters its DNA binding functions. *J. Biol. Chem.*, **273**, 11839–11843.
47. Hellman,L.M. and Fried,M.G. (2007) Electrophoretic mobility shift assay (EMSA) for detecting protein-nucleic acid interactions. *Nat. Protoc.*, **2**, 1849–1861.
48. Bullock,A.N., Henckel,J., DeDecker,B.S., Johnson,C.M., Nikolova,P.V., Proctor,M.R., Lane,D.P. and Fersht,A.R. (1997) Thermodynamic stability of wild-type and mutant p53 core domain. *Proc. Natl. Acad. Sci. U.S.A.*, **94**, 14338–14342.
49. Friedler,A., Veprintsev,D.B., Hansson,L.O. and Fersht,A.R. (2003) Kinetic instability of p53 core domain mutants: implications for rescue by small molecules. *J. Biol. Chem.*, **278**, 24108–24112.
50. Joerger,A.C. and Fersht,A.R. (2010) The tumor suppressor p53: from structures to drug discovery. *Cold Spring Harbor Perspect. Biol.*, **2**, a000919.
51. Kypr,J., Kejnovská,I., Renčiuk,D. and Vorlíčková,M. (2009) Circular dichroism and conformational polymorphism of DNA. *Nucleic Acids Res.*, **37**, 1713–1725.
52. Follmann,H., Kuntz,I. and Zacharias,W. (1975) Adenine nucleosides in Solution: Circular dichroism studies and base conformation. *Eur. J. Biochem.*, **58**, 31–41.
53. Nielsen,S.B., Chakraborty,T. and Hoffmann,S.V. (2005) Synchrotron radiation circular dichroism spectroscopy of ribose and deoxyribose sugars, adenosine, AMP and dAMP nucleotides. *ChemPhysChem*, **6**, 2619–2624.
54. Sprecher,C.A. and Johnson,W.C. (1977) Circular dichroism of the nucleic acid monomers. *Biopolymers*, **16**, 2243–2264.
55. Vetri,V. and Foderà,V. (2015) The route to protein aggregate superstructures: Particulates and amyloid-like spherulites. *FEBS Lett.*, **589**, 2448–2463.
56. Vetri,V., Canale,C., Relini,A., Librizzi,F., Militello,V., Gliozzi,A. and Leone,M. (2007) Amyloid fibrils formation and amorphous aggregation in concanavalin A. *Biophys. Chem.*, **125**, 184–190.
57. Vetri,V., Leone,M., Morozova-Roche,L.A., Vestergaard,B. and Foderà,V. (2013) Unlocked concanavalin A forms Amyloid-like fibrils from coagulation of Long-lived "Crinkled" intermediates. *PLoS One*, **8**, e68912.
58. Ano Bom,A.P.D., Rangel,L.P., Costa,D.C.F., de Oliveira,G.A.P., Sanches,D., Braga,C.A., Gava,L.M., Ramos,C.H.I., Cepeda,A.O.T., Stumbo,A.C. *et al.* (2012) Mutant p53 aggregates into Prion-like amyloid oligomers and fibrils: implications for cancer. *J. Biol. Chem.*, **287**, 28152–28162.
59. Ishimaru,D., Andrade,L.R., Teixeira,L.S.P., Quesado,P.A., Maiolino,L.M., Lopez,P.M., Cordeiro,Y., Costa,L.T., Heckl,W.M., Weissmüller,G. *et al.* (2003) Fibrillar aggregates of the tumor suppressor p53 core domain. *Biochemistry*, **42**, 9022–9027.
60. Lee,A.S., Galea,C., DiGiammarino,E.L., Jun,B., Murti,G., Ribeiro,R.C., Zambetti,G., Schultz,C.P. and Kriwacki,R.W. (2003)

Reversible amyloid formation by the p53 tetramerization domain and a cancer-associated mutant. *J. Mol. Biol.*, **327**, 699–709.
61. Vuzman,D., Azia,A. and Levy,Y. (2010) Searching DNA via a "Monkey Bar" mechanism: the significance of disordered tails. *J. Mol. Biol.*, **396**, 674–684.
62. Fuxreiter,M., Simon,I. and Bondos,S. (2011) Dynamic protein-DNA recognition: beyond what can be seen. *Trends Biochem. Sci.*, **36**, 415–423.
63. Vuzman,D. and Levy,Y. (2012) Intrinsically disordered regions as affinity tuners in protein–DNA interactions. *Mol. Biosyst.*, **8**, 47–57.
64. Altmeyer,M., Neelsen,K.J., Teloni,F., Pozdnyakova,I., Pellegrino,S., Grofte,M., Rask,M.-B.D., Streicher,W., Jungmichel,S., Nielsen,M.L. *et al.* (2015) Liquid demixing of intrinsically disordered proteins is seeded by poly(ADP-ribose). *Nat.Commun.*, **6**, 8088.
65. Agarwal,M.L., Agarwal,A., Taylor,W.R., Wang,Z.Q., Wagner,E.F. and Stark,G.R. (1997) Defective induction but normal activation and function of p53 in mouse cells lacking poly-ADP-ribose polymerase. *Oncogene*, **15**, 1035–1041.
66. Vivelo,C.A., Wat,R., Agrawal,C., Tee,H.Y. and Leung,Anthony K L. (2017) ADPriboDB: The database of ADP-ribosylated proteins. *Nucleic Acids Res.*, **45**, D204–D209.
67. Laptenko,O. and Prives,C. (2006) Transcriptional regulation by p53: one protein, many possibilities. *Cell Death Differ.*, **13**, 951–961.
68. D'Abramo,M., Besker,N., Desideri,A., Levine,A.J., Melino,G. and Chillemi,G. (2016) The p53 tetramer shows an induced-fit interaction of the C-terminal domain with the DNA-binding domain. *Oncogene*, **35**, 3272–3281.
69. Petty,T.J., Emamzadah,S., Costantino,L., Petkova,I., Stavridi,E.S., Saven,J.G., Vauthey,E. and Halazonetis,T.D. (2011) An induced fit mechanism regulates p53 DNA binding kinetics to confer sequence specificity. *EMBO J.*, **30**, 2167–2176.
70. Wang,Y., Rosengarth,A. and Luecke,H. (2007) Structure of the human p53 core domain in the absence of DNA. *Acta Crystallogr. D, Biol. Crystallogr.*, **63**, 276–281.
71. Kitayner,M., Rozenberg,H., Kessler,N., Rabinovich,D., Shaulov,L., Haran,T.E. and Shakked,Z. (2006) Structural basis of DNA recognition by p53 tetramers. *Mol. Cell*, **22**, 741–753.
72. Arlt,C., Ihling,C.H. and Sinz,A. (2015) Structure of full-length p53 tumor suppressor probed by chemical cross-linking and mass spectrometry. *Proteomics*, **15**, 2746–2755.
73. Yue,X., Zhao,Y., Xu,Y., Zheng,M., Feng,Z. and Hu,W. (2017) Mutant p53 in cancer: accumulation, gain-of-function, and therapy. *J. Mol. Biol.*, **429**, 1595–1606.
74. Kim,M.P. and Lozano,G. (2017) Mutant p53 partners in crime. *Cell Death Differ.*, **25**, 161.
75. Mora,P., Carbajo,R.J., Pineda-Lucena,A., Sanchez del Pino,M.M. and Perez-Paya,E. (2008) Solvent-exposed residues located in the beta-sheet modulate the stability of the tetramerization domain of p53–a structural and combinatorial approach. *Proteins*, **71**, 1670–1685.